Journal of Sound and Vibration 482 (2020) 115460

Contents lists available at ScienceDirect

Journal of Sound and Vibration

journal homepage: www.elsevier.com/locate/jsvi

Characterization of challenges in asymmetric nonlinear vibration energy harvesters subjected to realistic excitation

Wen Cai, Ryan L. Harne*

Department of Mechanical and Aerospace Engineering, The Ohio State University, Columbus, OH, 43210, USA

ARTICLE INFO

Article history:
Received 10 December 2019
Received in revised form 17 April 2020
Accepted 14 May 2020
Available online 19 May 2020
Handling Editor: 2EPAV- Pavlovskaia

Keywords:
Equivalent linearization method
Asymmetry
Combined harmonic and stochastic excitation
Nonlinear dynamics
Direct current voltage

ABSTRACT

With an explosion of the internet of things (IoT), vibration energy harvesting provides an environmentally friendly solution to replace consumable batteries in powering IoT wireless sensors. Yet, when implemented in practice, ambient vibration input energy is much less periodic than assumptions adopted in previous studies. This becomes especially important given that asymmetries are inevitable in nonlinear device platforms. This research sheds light on these complex challenges of practical vibration energy harvesting by developing and exploring an analytical model based on equivalent linearization. The modeling approach provides an opportunity to understand influences of asymmetry, nonlinearity, and combined excitation response on the DC power delivery of energy harvesters. In the analytical model, a weighted Gaussian joint distribution is utilized to approximate the influences caused by the random excitation. Combined with numerical and experimental validation, the analysis indicates that with the increase of stochastic base acceleration, two outcomes are possible. A first outcome involves an enhancement of DC power by way of triggering large amplitude nonlinear oscillations. A second outcome corresponds to a loss of high power delivery since the noise interferes with the attainment of the snap-through dynamic. Either reducing asymmetry or increasing harmonic excitation component is found to be favorable to induce the power-enhancing dynamics and inhibit the occurrence of the second case. Although with the simplified Gaussian distribution, the analytical framework cannot reproduce exact details of the dynamic responses in every case, the results show that the statistical trends of the analysis are overall borne out in simulation and experiment. This indicates the new modeling of this research may help guide attention to design and deployment techniques for nonlinear vibration energy harvesters in practical combined excitation environments, where limitations on precise manufacture or placement may introduce structural asymmetry.

1. Introduction

The extensive network of interconnected wireless devices termed the Internet-of-Things (IoT) has been widely built up in recent years for applications such as building operations [1], healthcare [2], and smart farming [3], to name a few. The IoT results in smart, data-informed strategies by continuously collecting and processing trends of user consumption, system health, and other important metrics. With a projected increase of IoT devices to a trillion by 2025 [4], the high demand on

* Corresponding author.
E-mail address: harne.3@osu.edu (R.L. Harne).

https://doi.org/10.1016/j.jsv.2020.115460
0022-460X/

disposable batteries suggests a clear threat to the sustainability of our environment and infrastructure. With the decrease of required power for IoT devices to microwatts [4], vibration energy harvesting can be an environmentally friendly energy provider of on-demand electrical power due to the high power density and broad availability of kinetic energy [5].

In recent years, numerous research efforts have been devoted to improving the performance of vibration energy harvesting systems. Because of the narrowband characteristic of linear vibration energy harvesters, nonlinear energy harvesting systems are proposed to meet the requirements of broadband frequency sensitivity and high output power resulting from the input vibration energy [6–9]. Because of the multistability feature of energy harvesters with particular nonlinearities, a wide variety of methods have been proposed to readily attain high energy orbit vibration [10–12]. For example, Zhou et al. [12] proposed a flexible bistable energy harvester with a controllable potential energy function that helps one govern the potential energy barrier for triggering snap-through vibration. Wang and Liao [11] utilized the load perturbation method to create strategies that transform system states from intrawell vibration to snap-through oscillation.

In addition, optimization strategies are applied seeking energy harvesting system designs with maximized performance [13–15]. Dietl and Garcia [16] employed a gradient search optimization tool to determine that a curved beam shape along the beam length axis provides optimal and uniform strain distribution for power maximization. Cai and Harne [17,18] utilized the genetic algorithm optimization method to uncover the entangled influences of nonlinearity, beam shape, and tip mass for high performing and structurally resilient energy harvesting cantilever designs. Since rectification is necessary to convert the alternating current (AC) voltage from the piezoelectric beam to direct current (DC) voltage, studies on harvesting circuits explore methods for maximizing power delivery [19,20]. By utilizing switching strategies with standard rectification, the synchronous electric charge extraction (SECE) circuit was found to yield a 400% increase in harvested power [21]. On the basis of the SECE circuit, Lefeuvre et al. [22] presented a phase-shift SECE (PS-SECE) circuit to improve the delivered power up to a theoretical limit for piezoelectric devices having high electromechanical coupling.

From this survey of state-of-the-art investigations, one common assumption adopted is the symmetry of potential energy functions when leveraging nonlinearities for energy harvesting [7,8,17]. Yet, due to factors such as asymmetric magnetic fields, structure imperfections, or static and gravitational loads, asymmetry is nearly unavoidable in implementing nonlinear energy harvesting systems. This indicates it is necessary to investigate the influences of asymmetry in the development of nonlinear energy harvesters. He and Daqaq [23] examined the AC output power of asymmetric nonlinear energy harvesting systems subjected to pure white noise excitation vibration and indicated that the existence of asymmetry may increase the output power for a monostable system, whereas the performance of a bistable system is deteriorated. Wang et al. [24] introduced an installation bias angle to asymmetric bistable energy harvesting systems to reduce negative effects caused by asymmetric potentials for the energy harvesters when subjected to pure harmonic or random excitation.

Moreover, pure harmonic or pure stochastic excitation is usually employed in studies to characterize electrodynamic responses [25,26]. In fact, environments wherein harvesters may be employed to sustain IoT devices may experience complex vibration conditions such as combined harmonic and stochastic excitation [27,28]. For instance, with the influence of moving vehicles, the vibrations of bridges show a combined influence of periodic oscillation and random vibration [28]. In order to analytically predict the dynamical characteristics when subjected to combined harmonic and stochastic excitation, methods such as Gaussian closure method [29,30], stochastic averaging method [31,32], and equivalent linearization method [33], have been applied to symmetric Duffing oscillators to statistically characterize the structural dynamics. Yet, due to the complicated mechanical-electrical coupling in energy harvesters, analytical approaches seldom address DC power delivery that results following rectification stages. A few insights on this class of structural-electrical coupling have been obtained. For instance, Kim et al. [34] used numerical approaches to identify the stochastic resonance phenomenon for rotating energy harvesting systems under combined harmonic and stochastic excitation and validated the findings by experiments. Dai and Harne [35] introduced an analytical approach to determine the relationship between the electrical and mechanical responses and thus predict the electromechanical responses of cantilevered energy harvesters due to combined harmonic and stochastic excitation. On the other hand, no works have synthesized a prediction tool for the intricate electromechanical responses of asymmetric nonlinear vibration energy harvesters subjected to combined vibration excitation conditions. The insight from such an analytical process would be strongly relevant to help transition energy harvesting devices to practice.

Motivated to fill the void in understanding, this research investigates the dynamic behaviors of an asymmetric nonlinear energy harvester integrated with a standard rectification circuit. The aim is to characterize the mechanical and electrical responses when subjected to combined harmonic and stochastic excitation. In the following sections, an analytical framework is first established for the proposed system. After validating the system numerically and experimentally, the influences of asymmetry are investigated considering the combined harmonic and stochastic excitation condition. Finally, a summary of main findings in the study is provided to conclude this report.

2. Analytical model formulation

The vibration energy harvesting platform considered in this study is shown in Fig. 1. A piezoelectric cantilever has a tip mass M_0 constructed by the magnet 1 and its holder at the free end. The beam is excited by base motion representative of the ambient kinetic energy. The electrodes of the beam are interfaced with a standard rectification circuit to convert the AC voltage to a DC voltage. A pair of repulsive magnets is utilized to introduce nonlinearities into the system. The gap d_2 and bias Δ between the two magnets determine the magnetic force F_m that governs the type of nonlinearity and the significance of

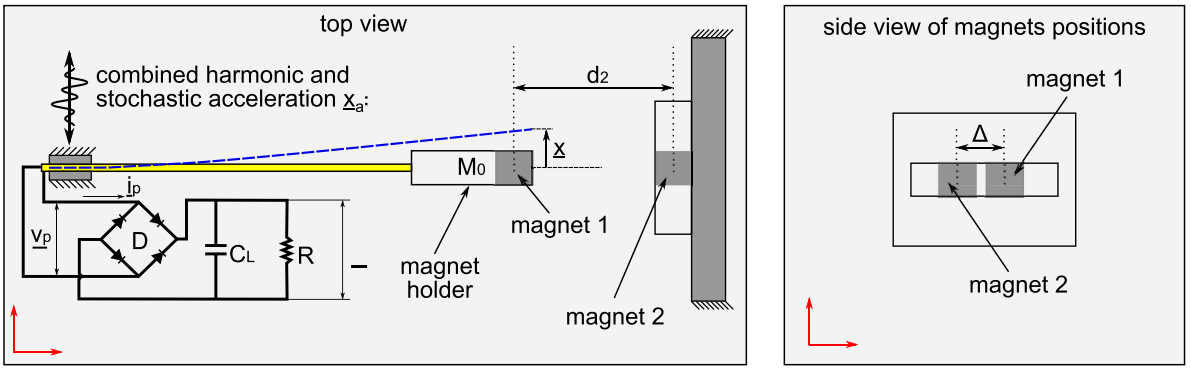

Fig. 1. Schematic of nonlinear energy harvesting system.

asymmetry induced into the potential energy profile of the system. The polynomial expression in Eq. (1) is adopted in the model to approximate the nonlinear magnetic force F_m [36,37]. The parameters k_1,k_2 and k_3 are experimentally identified, as described in Section 3.

$$F_m = k_1\underline{x} + k_2\underline{x}^2 + k_3\underline{x}^3 \tag{1}$$

Therefore, the non-dimensional equivalent lumped parameter governing equations for the lowest order structural and electrical responses are [23,35]:

$$x'' + \eta x' + (1-p)x + \beta_2 x^2 + \beta_3 x^3 + \kappa v_p = -x_a'' \tag{2a}$$

$$v_p' + i_p = \theta x' \tag{2b}$$

The relationships between the non-dimensional parameters with the physical system parameters are

$$x = \underline{x}/x_0;\ v_p = \underline{v}_p/V_0;\ \omega_0 = \sqrt{k/m};\ \tau = \omega_0 t;\ p = -k_1/k;\ \beta_2 = k_2 x_0/k;\ \beta_3 = k_3 x_0^2/k;\ \kappa = \alpha V_0/(kx_0);\ \eta = d/(m\omega_0);\ \theta = \alpha x_0/(C_p V_0);\ i_p = \underline{i}_p \omega_0/(C_p V_0);\ x_a'' = \ddot{\underline{x}}_a m/(x_0 k); \tag{3a-l}$$

Here, $\underline{x}$ is the beam tip displacement relative to the motion of the base displacement $\underline{x}_a$; m, d, and $k$are the equivalent lumped mass, viscous damping, and linear stiffness corresponding to the first mode of the beam vibration; p is the load parameter indicating the influence of magnetic forces on reducing the linear stiffness$k$; α is the electromechanical coupling constant; C_p is the internal capacitance of the piezoelectric layers in the cantilever; $\underline{v}_p$ is the voltage across the piezoelectric beam electrodes; $\underline{i}_p$ is the corresponding current through the harvesting circuit; x_0 and V_0 are characteristic length and voltage, which are 1 mm and 1 V respectively; The over dot and apostrophe operators indicate differentiation with respect to time t and non-dimensional time τ, respectively.

The non-dimensional combined harmonic and stochastic base acceleration is

$$-x_a'' = a\cos\omega\tau + \sigma w(\tau) \tag{4}$$

Here, the non-dimensional standard deviation of the stochastic acceleration is σ, while the amplitude of harmonic base excitation is a; ω is the non-dimensional angular frequency of the harmonic base excitation determined by $\omega = \underline{\omega}/\omega_0$; $\underline{\omega}$ is the absolute angular frequency; $w(\tau)$ is a unit Gaussian white noise process.

For the nonlinear structural system expressed by Eq. (2), the mean value of the displacement response x is defined to be m_x. Consequently, the displacement response x is represented by

$$x = x_0 + m_x \tag{5}$$

Here, x_0 is the zero mean dynamic response.

The equivalent linearization method [23,33,38] is applied to Eq. (2a) to linearize the quadratic and cubic nonlinearities by introducing the equivalent linear natural frequency ω_e and displacement offset ε.

$$x_0'' + \eta x_0' + \omega_e^2 x_0 + \varepsilon + \kappa v_p = -z'' \tag{6a}$$

$$v_p' + i_p = \theta x_0' \tag{6b}$$

In order to ensure the equivalence between Eq. (2) and Eq. (6), the mean-square error between (2) and (6) is minimized using (7a) and (7b) [23] [33] [35] [38].

$$\frac{\partial \langle E^2 \rangle}{\partial \omega_e^2} = \frac{\partial}{\partial \omega_e^2} \langle \left[(1-p)x + \beta_2 x^2 + \beta_3 x^3 - \omega_e^2 x_0 - \varepsilon \right]^2 \rangle = 0 \tag{7a}$$

$$\frac{\partial \langle E^2 \rangle}{\partial \varepsilon} = \frac{\partial}{\partial \varepsilon} \langle \left[(1-p)x + \beta_2 x^2 + \beta_3 x^3 - \omega_e^2 x_0 - \varepsilon \right]^2 \rangle = 0 \tag{7b}$$

The bracket $\langle\rangle$ indicates the mathematical expectation or time-averaged value. By calculating the mean value for both sides of Eq. (6a), it is found that $\varepsilon = 0$.

Based on the linearized system Eq. (6) with equivalent frequency ω_e and offset ε determined through the Eq. (7), superposition is applied. Here, the total structural and electrical responses are approximated to be the summation of responses individually attributed to the harmonic or stochastic excitation components.

$$x_0 = x_h + x_r \tag{8a}$$

$$v_p = v_{ph} + v_{pr} \tag{8b}$$

The x_h and v_{ph} represent the structural and electrical responses, respectively, of the equivalent linear system resulting from the harmonic excitation component, as governed by Eq. (9). The x_r and v_{pr} are the stochastic components of the displacement and voltage specifically governed by Eq. (10).

$$x_h'' + \eta x_h' + \omega_e^2 x_h + \kappa v_{ph} = a \cos \omega\tau \tag{9a}$$

$$v_{ph}' + i_{ph} = \theta x_h' \tag{9b}$$

$$x_r'' + \eta x_r' + \omega_e^2 x_r + \kappa v_{pr} = \sigma w(\tau) \tag{10a}$$

$$v_{pr}' + i_{pr} = \theta x_r' \tag{10b}$$

For the structural response x_h due to the harmonic excitation, the fundamental frequency ω of the base acceleration is assumed to be the dominant frequency of displacement. Thus the x_h is given by

$$x_h = h \sin \omega\tau + g \cos \omega\tau = n \cos(\omega\tau - \phi) \tag{11}$$

The corresponding piezoelectric voltage v_{ph} is represented by a piecewise function shown in Eq. (12) [35,39].

$$v_{ph} = \begin{cases} \theta n(\cos \omega\tau - 1) + V_{rh}; & 0 < \omega\tau \le \Theta \\ -V_{rh}; & \Theta < \omega\tau \le \pi \\ \theta n(\cos \omega\tau + 1) - V_{rh}; & \pi < \omega\tau \le \pi + \Theta \\ V_{rh}; & \pi + \Theta < \omega\tau \le 2\pi \end{cases} \tag{12}$$

The V_{rh} is the non-dimensional magnitude of the rectified voltage resulting from the load resistance R, shown in Fig. 1.

The magnitude of the rectified voltage is obtained by integrating Eq. (6b) over a semi-period of the harmonic excitation [35,40],

$$V_{rh} = \frac{2\theta n}{(\pi/\omega)\rho + 2}, \quad \rho = \frac{1}{C_p R \omega_0} \tag{13a, b}$$

Here, ρ is the non-dimensional resistance.

Consequently, the piezoelectric voltage v_{ph} is related to the lowest order displacement x_h and velocity x_h' by the fundamental term of a Fourier series of Eq. (12).

$$v_{ph} = \frac{A}{\omega} x_h' + B x_h \tag{14}$$

where

$$A = \frac{1}{\pi}\theta \sin^2\Theta\ ,\ B = \frac{1}{2\pi}\theta(2\Theta - \sin 2\Theta),\ \text{and}\ \cos\Theta = \frac{\pi - 2\omega\omega_0 C_p R}{\pi + 2\omega\omega_0 C_p R} \tag{15a,b,c}$$

The response x_h is achieved by substituting Eqs. (11) and (14) into Eq. (9a).

$$g = \frac{a\left(B\kappa - \omega^2 + \omega_e^2\right)}{\left(B\kappa - \omega^2 + \omega_e^2\right)^2 + (A\kappa + \eta\omega)^2};\quad h = \frac{a(A\kappa + \eta\omega)}{\left(B\kappa - \omega^2 + \omega_e^2\right)^2 + (A\kappa + \eta\omega)^2}; \tag{16a,b}$$

The corresponding electrical responses are also determined by Eqs. (13) and (14) following computation of Eq. (16).

For the stochastic responses governed by Eq. (10), based on the generalized harmonic function [41], the corresponding stochastic displacement x_r and velocity x_r' are written as

$$x_r = n_r \cos(\omega_r\tau + \phi_r) = h_r \sin\omega_r\tau + g_r \cos\omega_r\tau \tag{17a}$$

$$x_r' = -n_r\omega_r \sin(\omega_r\tau - \phi_r) = h_r\omega_r \cos\omega_r\tau - g_r\omega_r \sin\omega_r\tau \tag{17b}$$

Here ω_r and $n_r$are the angular frequency and amplitude for the periodic non-stationary process [25,41].

Consequently, the relationship shown in Eq. (14) is also applicable for stochastic components according to the frequency ω_r.

$$v_{pr} = \frac{A_r}{\omega_r} x_r' + B_r x_r \tag{18}$$

where

$$A_r = \frac{1}{\pi}\theta \sin^2\Theta_r,\ B_r = \frac{1}{2\pi}\theta(2\Theta_r - \sin 2\Theta_r),\ \text{and}\ \cos\Theta_r = \frac{\pi - 2\omega_r\omega_0 C_p R}{\pi + 2\omega_r\omega_0 C_p R} \tag{19a,b,c}$$

Substituting Eq. (19) into Eq. (10a), the equivalent mechanical governing equation under the stochastic excitation is obtained.

$$x_r'' + \left(\eta + \frac{A_r\kappa}{\omega_{nr}}\right)x_r' + \left(\omega_e^2 + \kappa B_r\right)x_r = \sigma w(\tau) \tag{20}$$

From Eq. (20), the non-stationary angular frequency is [42].

$$\omega_r = \sqrt{\left(\omega_e^2 + \kappa B_r\right)} \tag{21}$$

To determine the mean-square of the stochastic displacement component $\langle x_r^2 \rangle$ from Eq. (20), the probability density distribution must first be evaluated. Therefore, assuming a standard Gaussian distribution for x_r, the probability distribution for the random process x_r considering a mean displacement m_x is given by Eq. (22).

$$f(x_{rm}) = g\left(x_{rm}|m_x, \sigma_{xg}\right) = \frac{1}{\sigma_{xg}\sqrt{2\pi}} e^{-\frac{1}{2}\left(\frac{x_{rm} - m_x}{\sigma_{xg}}\right)^2} \tag{22a}$$

$$\sigma_{xg} = \frac{\sigma}{\sqrt{2\left(\eta + \frac{A_r\kappa}{\omega_{nr}}\right)\left(\omega_e^2 + \kappa B_r\right)}} \tag{22b}$$

Here, x_{rm} is the summation of x_r and m_x, σ_{xg} is the non-dimensional standard deviation of x_{rm} associated with the standard Gaussian distribution and determined by Eq. (22b).

Yet, for nonlinear systems with multiple static equilibria, a standard Gaussian distribution assumption for the random variable $x_r$does not provide good approximation of observable response statistics [43]. Therefore, in order to improve the accuracy in the analytical predictions, a weight w_e is introduced to formulate a weighted Gaussian distribution in Eq. (23).

$$f_1(x_{rm}) = g(x_{rm}|m_x, \sigma_{xw}) = g(x_{rm}|m_x, w_e\sigma_{xg}) \tag{23}$$

The σ_{xw} corresponds to the standard deviation of x_{rm} associated with the weighted Gaussian distribution. In other words, $\sigma_{xw} = w_e\sigma_{xg}$, where the weight w_e is a product with the non-dimensional standard deviation σ_{xg} of x_{rm}.

In order to determine the weight, a probability density distribution for nonlinear systems under pure stochastic excitation with multiple stable equilibria is given in Eq. (24) [43] against which the weighted Gaussians Eq. (23) are compared ignoring the influence of harmonic excitation.

$$f_2(x_{rm}) = \frac{1}{2}g\left(x_{rm}|x_1, \sigma_{xg}\right) + \frac{1}{2}g\left(x_{rm}|x_2, \sigma_{xg}\right) \tag{24}$$

Here in Eq. (24) the $g(x_{rm}|x_1, \sigma_{xg})$ and $g(x_{rm}|x_2, \sigma_{xg})$ are standard Gaussian distributions with mean values of x_1 and x_2, such that x_1 and x_2 are the statically stable equilibria of the nonlinear system. To simplify the following discussion, the radicand in Eq. (22b) is considered to be a unit valued constant towards determining the suitable weight w_e.

Fig. 2 presents the probability density distributions given by Eqs. (23) and (24). For the probability distribution shown in Eq. (24) f_2, at noise standard deviation $\sigma = 0.1$ in Fig. 2(a), the two peak values are thoroughly separated, which indicates that snap-through vibration rarely occurs as caused by the random excitation component. This is because snap-through vibration is indicative of a zero mean value. With the increase of noise standard deviation to 0.8 as shown in Fig. 2(b), the two peaks begin to coalesce, which indicates that stochastic excitation may trigger snap-through vibration more often. At much higher noise standard deviation, Fig. 2(c) reveals that the two peaks merge so that there is high probability that the mean of the displacement is zero, corresponding to snap-through vibration.

For the distribution shown in Eq. (23) f_1, two weights are selected, $w_e = 1$ and $w_e = 2$ for evaluation in Fig. 2. When the noise intensity is too low to trigger snap-through vibrations, Fig. 2(a) shows that the mean value m_x is statistically identical to the value of the equilibria. Yet, for increase in the noise standard deviation σ, such as the values $\sigma = 0.8$ and $\sigma = 1.5$ in Fig. 2(b and c), snap-through vibration happens more frequently and the mean value m_x takes the mean of the two equilibrium positions, which is approximately zero.

As shown through the results of Fig. 2, the distribution of Eq. (23) f_1 may sufficiently reproduce the probability distribution of the exact nonlinear system based on the use of weight w_e. Compared with the distributions f_2 determined by Eq. (24), the weight $w_e = 2$ applied to distribution f_1 leads to a sufficient approximation of the peak value of the probability density function f_2.

To quantify the agreement of the distributions, Table 1 summarizes the mean-square values of the non-dimensional displacement by numerically integrating the expressions Eqs. (23) and (24). At low noise intensity in Fig. 2(a), the integral interval is chosen to be [-1.5, 1.5]. In comparison, for noise intensities in Fig. 2(b and c), the range [-3, 3] is selected. The relative errors of the approximated distributions f_1 with respect to the accurate distribution f_2 are provided in Table 1. It is observed that the distributions f_1 adequately approximate the distribution f_2 when the noise standard deviation is $\sigma = 0.1$ or $\sigma = 1.5$. Yet, for the intermediate standard deviation of stochastic excitation $\sigma = 0.8$, at which point Fig. 2 shows that the two peaks of statistical response coalesce, the weighted Gaussian distribution f_1 with the weight $w_e = 2$ better agrees with the accurate distribution f_2.

With the probability density distribution given in Eq. (24), the mean square value for the variable x_{rm} can be calculated by the Gaussian closure method when subjected to pure stochastic excitation [43]. Yet, when considering the combined harmonic and stochastic excitation, there is no direct way to establish an analytical expression for the mean square value of x_{rm} without an assumption for the Gaussian distribution [44]. Therefore, in the study the weighted Gaussian distribution f_1 with

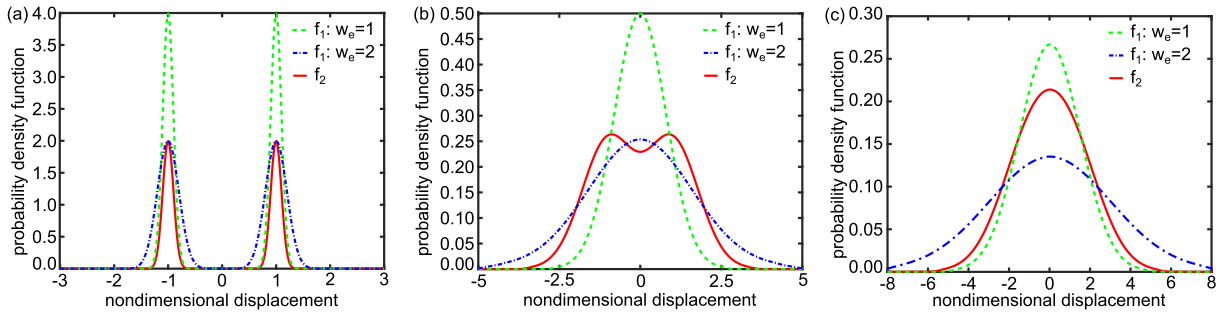

Fig. 2. Probability density distributions for standard deviations of stochastic base acceleration of (a) $\sigma = 0.1$, (b) $\sigma = 0.8$, and (c) $\sigma = 1.5$.

Table 1
Mean-square value of non-dimensional displacement at three non-dimensional noise standard deviations.

Noise standard deviation	$f_1: w_e = 1$		$f_1: w_e = 2$		f_2
	Mean-square displacement value	Relative error	Mean-square displacement value	Relative error	Mean-square displacement value
$\sigma = 0.1$	1.0010	2.32%	1.0010	2.32%	1.0248
$\sigma = 0.8$	0.6382	59.45%	1.7440	10.82%	1.5737
$\sigma = 1.5$	1.6617	13.58%	1.7887	7.34%	1.9229

$w_e = 2$ in Eq. (23) is chosen to balance the accuracy and simplicity in predicting the statistical responses analytically. The analytical expression for the mean values of random variable x_r is then given in Eq. (25), where $w_e = 2$.

$$\langle x_r^2 \rangle = \frac{(w_e \sigma)^2}{2\left(\eta + \frac{A_r K}{\omega_{nr}}\right)\left(\omega_e^2 + \kappa B_r\right)} \tag{25}$$

The corresponding mean-square rectified voltage is approximated from Eq. (13) to be

$$< v_r^2 > = \frac{4\theta^2 \omega_{nr}^2 \langle x_r^2 \rangle}{\pi^2 \rho^2 + 4\omega_{nr}^2 + 4\pi\rho\omega_{nr}} \tag{26}$$

Assuming the relationships in Eq. (27), the expressions for ω_e^2 and ε are determined by substitution and simplification of the Eqs. (5), (8) and (11) into Eq. (7). The squared equivalent frequency ω_e^2 and offset ε are given in Eq. (28).

$$\langle x_r \rangle = 0; \;\; \langle x_r^2 \rangle = \langle x_r^2 \rangle; \;\; \langle x_r^3 \rangle \approx 0; \;\; \langle x_r^4 \rangle \approx 3\langle x_r^2 \rangle^2; \tag{27}$$

$$\omega_e^2 = \frac{1}{(2\langle x_r^2 \rangle + n^2)} \left(\begin{array}{l} 2\langle x_r^2 \rangle + n^2 - 2\langle x_r^2 \rangle p - n^2 p + 6\langle x_r^2 \rangle^2 \beta_3 + 6\langle x_r^2 \rangle m_x^2 \beta_3 + 6\langle x_r^2 \rangle n^2 \beta_3 + \\ 3m_x^2 n^2 \beta_3 + \dfrac{3n^4 \beta_3}{4} + 4\langle x_r^2 \rangle m_x \beta_2 + 2m_x n^2 \beta_2 \end{array} \right) \tag{28a}$$

$$\varepsilon = m_x - m_x p + m_x^3 \beta_3 + \frac{3}{2} m_x n^2 \beta_3 + 3m_x \langle x_r^2 \rangle \beta_3 + m_x^2 \beta_2 + \frac{1}{2} n^2 \beta_2 + \langle x_r^2 \rangle \beta_2 \tag{28b}$$

Studying the expressions of ω_e^2 and ε in Eq. (28), despite the perceived independence of the harmonic structural response x_h and the stochastic structural response x_r, mutual influences exist through the coupling between harmonic and stochastic components evident in the equivalent linearized parameters in Eq. (28). Consequently, Eqs. (16), (25) and (28) are solved simultaneously. The corresponding electrical responses are then determined based on Eqs. (13) and (26). Due to the contribution from the stochastic base acceleration, the total mean-square value of converted voltage shown in Eq. (29) is taken to characterize the energy harvesting output in the following investigations.

$$\langle v_r^2 \rangle = v_{rh}^2 + \langle v_{rr}^2 \rangle \tag{29}$$

3. Experimental systems identification

The experimental platform is shown in Fig. 3. A piezoelectric beam with parallel-wired PZT layers (PPA-2014; Mide Technology) is clamped to an aluminum base, which is affixed to the electrodynamic shaker table (APS Dynamics 400). At the free end of the beam, magnet 1 is secured in an aluminum magnet holder connected to the beam tip. The nonlinearity and asymmetry included in the system are adjusted by the position of magnet 2 in relation to magnet 1. Two displacement lasers (Micro-Epsilon ILD-1420) are utilized to measure the absolute displacement of the shaker table and beam tip. The electrodynamic shaker table is driven by an amplifier (Crown XLS 2500) fed appropriate combinations of harmonic and stochastic excitation voltage. An accelerometer (PCB Piezotronics 333B40) on the shaker table is used to confirm the frequency content of the resulting base acceleration. A standard rectifier bridge (1N4148 diodes) is connected to the piezoelectric beam to convert the alternate current to direct current signal. Following the bridge, a smoothing capacitor C_r and resistive load R are utilized to quantify the harvested electric energy.

For the experimental platform in Fig. 3, classical relations are first employed to determine the lumped mass m and linear stiffness k of the lowest order displacement response [45]. The two static equilibrium positions x_1 and x_2, and the corresponding natural frequencies ω_{n1} and ω_{n2} are identified by impulsive ring-down evaluations. The viscous damping ratio is

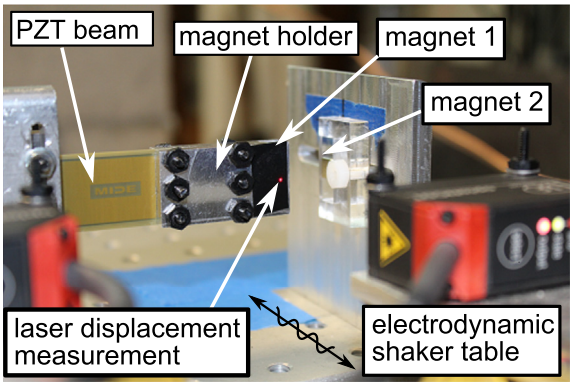

Fig. 3. Photo of experimental platform.

then calculated by the logarithmic decrement method. With these values determined and measured, the nonlinear stiffness parameters are calculated by Eq. (30).

$$k_2 = \frac{-m(\omega_{n1}^2 - \omega_{n2}^2)}{x_1 - x_2}; \quad k_3 = \frac{m(\omega_{n1}^2 - \omega_{n2}^2)}{x_1^2 - x_2^2}; \quad p = 1 + \frac{k_2}{k_1}x_1 + \frac{k_3}{k_1}x_1^2 = 1 + \frac{k_2}{k_1}x_2 + \frac{k_3}{k_1}x_2^2 \tag{30 a,b,c}$$

In order to comprehensively examine the influence of noise and asymmetry in the following report, three energy harvesting systems are selected. System 1 is a symmetrical system, and the other two systems have different extents of asymmetry. The identified system parameters are presented in Table 2. In the experiments, the resistance is fixed at 100 kΩ to ensure the circuit working in the optimal condition. The detailed influence of resistance on the rectified power can be found in the references [20,46].

4. Analytical model validation and discussion

The combined harmonic and stochastic excitation is applied to drive the energy harvesting system to validate the analytical model and characterize the electromechanical responses of the three nonlinear system configurations shown in Table 2. In the following investigations, the harmonic amplitude contribution to the base acceleration is 3.3 m/s^2 at frequencies of 9 Hz for system 1 and 2 and 10 Hz for system 3. The standard deviation of the stochastic base acceleration component is changed over the range of 0–1.6 m/s^2. To numerically simulate the responses, the fourth-order stochastic Runge-Kutta numerical method [47] is utilized, using 15 normally distributed and randomly selected initial conditions under each specific combination of the harmonic and stochastic base acceleration. The simulation duration is 8000 harmonic periods. In experiments, the duration of measurements is also 8000 harmonic periods. In order to replicate varying initial conditions experimentally, impulsive disturbances may be applied to the beam tip at the start of a given test. The impulses are empirically found to be around 5 kg mm/s.

With the parameters shown in Table 2, each nonlinear system exhibits two stable equilibria. This distinction leads to three classes of vibration: (i) large amplitude snap-through vibration that jumps between two equilibria, (ii) small amplitude intrawell vibration that vibrates around one equilibrium position, and (iii) aperiodic vibration that cannot coexist with the other two types at a certain frequency. Since aperiodic vibration cannot be predicted through the analytical method, this study focuses on the snap-through and intrawell vibration to examine dynamical characteristics resulting from combined harmonic and stochastic excitation. Detailed information about the three vibration types can be found in the reference [48].

Dynamical characteristics of the symmetrical nonlinear energy harvesting system.

The symmetrical nonlinear system 1 is first considered with the parameter $\Delta = 0$. The analytical and numerical results of the mean value of displacement and the mean-square of rectified voltage are shown in Fig. 4(a,c) for noise standard deviations

Table 2
Identified system parameters for three nonlinear systems studied in this research.

	m(g)	p(dim)	k_1(N/m)	k_2(kN/m^2)	k_3(MN/m^3)	d(N• s/m)	α(mN/V)	C_p(nF)	R(kΩ)
System 1	18.17	1.18	556	0	24	0.15	1.1	88	100
System 2	18.17	1.18	556	4	23	0.15	1.1	88	100
System 3	18.17	1.16	556	27	26	0.15	1.1	88	100

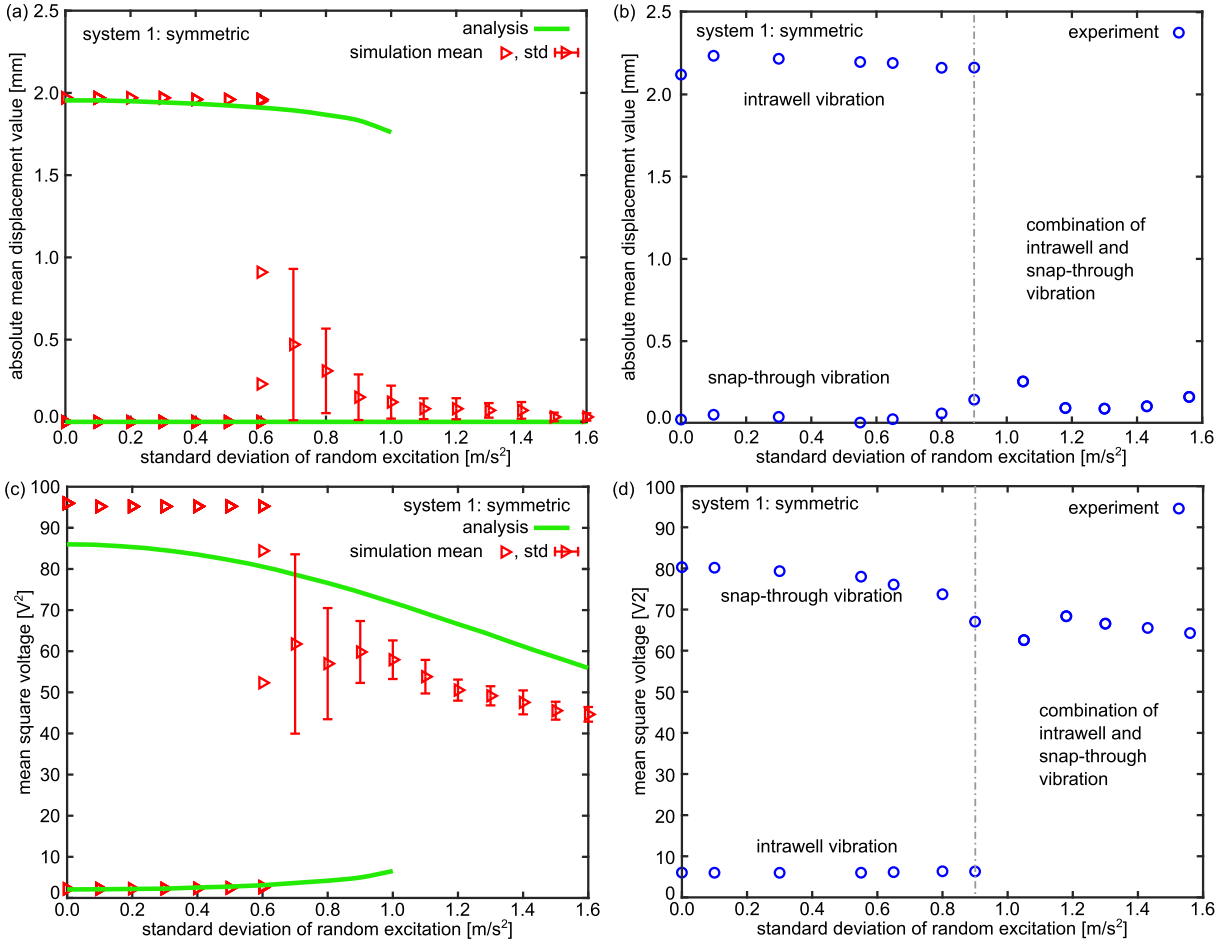

Fig. 4. Responses for system 1 with harmonic base acceleration amplitude 3.3 m/s^2 at frequency 9 Hz. Absolute mean value of displacement amplitude from (a) analysis and simulation and (b) experiment. Mean-square of total rectified voltage from (c) analysis and simulation and (d) experiment.

from 0 to 1.6 m/s^2. At low noise intensity, specifically less than 0.6 m/s^2, because the standard deviation is larger than half of the mean value, the numerical results are shown with the original simulation data. Otherwise, the mean value and standard deviation are used to statistically show the numerical results, which holds for all simulation plots throughout this report. As shown in Fig. 4(a,c), depending on the initial conditions, the system is seen to realize either snap-through or intrawell vibration for small standard deviations of the stochastic base acceleration component. These distinct behaviors are validated experimentally in Fig. 4(b,d). In experiments, the noise standard deviation does not distribute uniformly because of the filter used in generating excitation signals in experiments. In addition, the beam uses a glass-reinforced epoxy layers in the laminate sequence [17]. This leads to inevitable viscoelastic creep so that the mean displacement values increase with time in experiments, especially for the intrawell vibration as shown in Fig. 5(a). Therefore, the mean displacement values measured from experiments vary when the standard deviation of noise varies and is higher than the mean displacement value calculated from the analysis and simulation. Besides, due to the electrical losses in the rectification circuit that are not accounted for in the models, the measured mean-square rectified voltage is less than analytical and numerical results. Yet, overall, both the qualitative and quantitative range of behaviors observed for the symmetrical nonlinear energy harvesting system excited by the combined harmonic and stochastic base accelerations are in good agreement for lower standard deviations of the noise.

Considering the cases for when the standard deviation of the stochastic base acceleration is around 1 m/s^2, Fig. 4(a,c) show that the numerical results indicate regular fluctuations between the snap-through and intrawell vibration levels in terms of the mean displacement and the mean-square rectified voltage. Comparatively, the analysis results in mean-square voltages that appear to follow the average behavior of the simulation trends. Yet, for noise intensity greater than around 1 m/s^2, the dependence of the electromechanical responses on the initial conditions is reduced. For much greater noise standard deviation around 1.6 m/s^2, the mean values of displacement amplitude in Fig. 4(a) are close to the value of snap-through vibration and the standard deviation approaches zero. Temporal snap-shots of the beam tip displacement are given in Fig. 5(b)

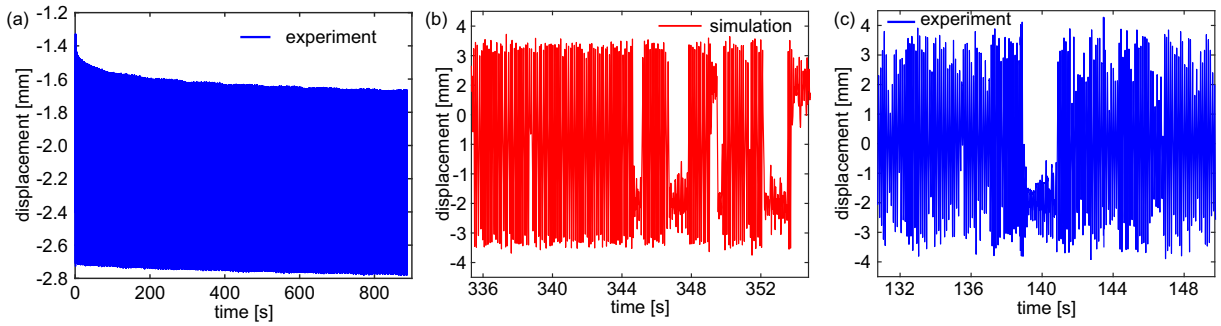

Fig. 5. Transient displacements from (a) experiment under pure harmonic excitation, (b) simulation and (c) experiment at harmonic excitation amplitude 3.3 m/s^2 and noise standard deviation 1.6 m/s^2.

to reveal that the behavior is dominated by snap-through between equilibria, which decreases the mean displacement value in the way shown through Fig. 4(a). In experiments Fig. 4(b,d), when the noise standard deviation is greater than around 1 m/s^2, the system only responds with a combination of intrawell and snap-through vibration as seen through the transient response in Fig. 5(c). The analysis agrees with these trends qualitatively and quantitatively, furthermore revealing good statistical estimates of the mean-square rectified voltage also observed numerically and experimentally.

The trends observed through Fig. 4 are similar to the influence of noise standard deviation demonstrated in Fig. 2 that at high noise standard deviation the snap-through vibration happens much more frequently and becomes the dominant vibration type in the responses. In addition, such trends can also be explained through the perspective of potential energy shapes. Since the equivalent linearized model natural frequency ω_e is in part governed by the stochastic displacement contribution, the stochastic base acceleration has influences on the equivalent potential energy function. Here, Eq. (6) is used to determine the potential energy function associated with noise as shown in Fig. 6. Without noise, a double-well potential energy profile is formed, corresponding to a bistable system configuration. With the noise standard deviation added to 1.6 m/s^2, the depth of the potential well shallows to make snap-through vibration happens more frequently. Further increasing the noise standard deviation to 4.8 m/s^2, the potential energy function resembles a monostable system with one global minimum, corresponding to a stable equilibrium configuration around which the energy harvester oscillates. This explains the occurrence of snap-through-like vibration with the greater noise components to the base acceleration.

Dynamical characteristics of asymmetrical nonlinear energy harvesting systems.

On the basis of system 1, the magnet 2 is repositioned to set the distance Δ of 0.02 mm, which is termed system 2. Further moving the magnet 2 to increase the distance Δ to be around 0.05 mm, the system 3 is constructed. Based on the potential energy plots shown in Fig. 7, the potential energy difference between the two potential wells for system 2 is around 20%. Comparatively, for system 3, such difference is increased to 77%. Therefore, in the following discussion, systems 2 and 3 are respectively termed as slight and large asymmetrical systems.

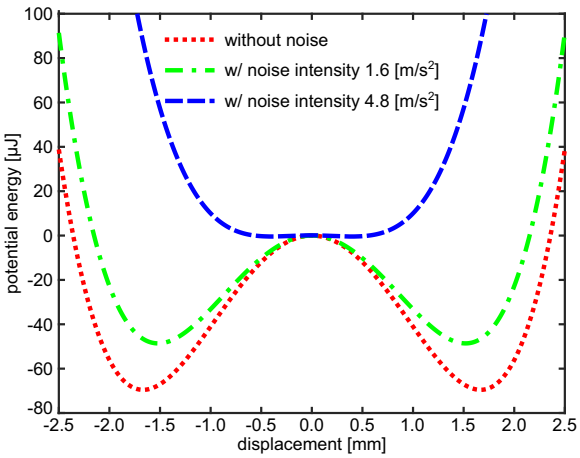

Fig. 6. Potential energy from linearized governing equation accounting for changes in noise intensity.

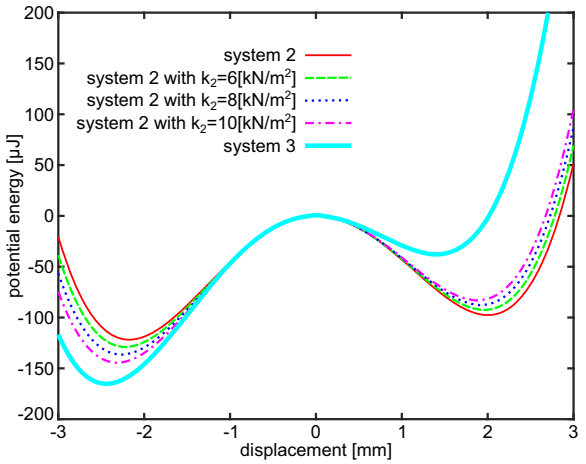

Fig. 7. Potential energy profiles for the asymmetrical energy harvesting systems.

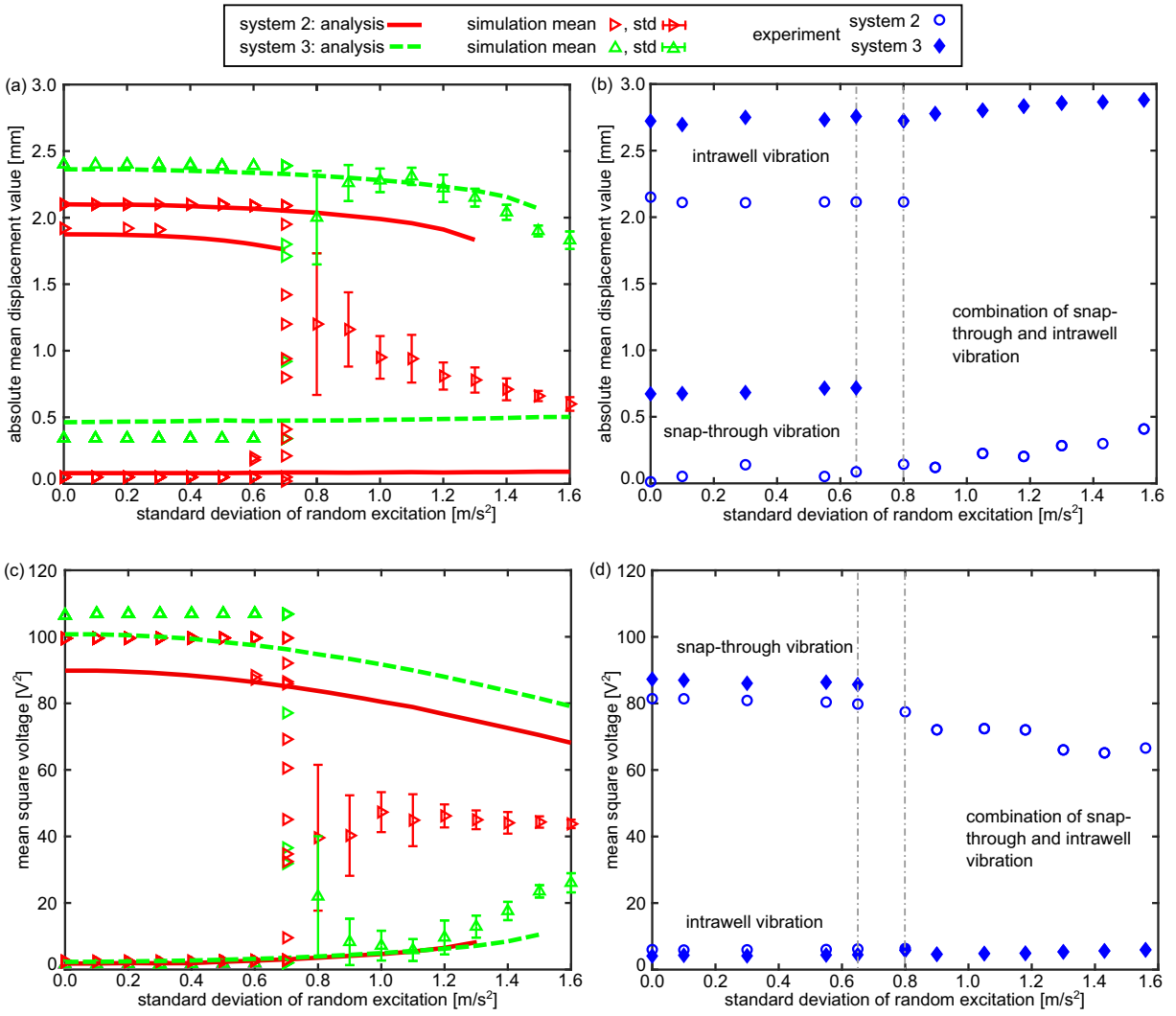

Fig. 8. Responses for systems 2 and 3 with harmonic amplitude 3.3 m/s^2 at frequency 9 Hz and 10 Hz. Absolute mean value of displacement amplitude from (a) analysis and simulation and (b) experiment. Mean-square of total rectified voltage from (c) analysis and simulation and (d) experiment.

Considering the range of combined harmonic and stochastic base acceleration, the mean value of displacement and mean-square rectified voltage from analysis and simulation are shown in Fig. 8(a,c), while the corresponding experimental data is shown in Fig. 8(b,d). As also observed for the symmetrical system 1, two types of response may either occur for two asymmetrical systems at small noise standard deviation such as less than 0.7 m/s^2, as seen in Fig. 8. Yet, when the noise intensity is above 0.8 m/s^2, the existence of noise has different influences on responses for two asymmetrical systems. For slight asymmetrical system 2, similar to the trends demonstrated in Fig. 4, with the increase of noise intensity, the mean displacement value in simulation is decreased 75% with a near zero standard deviation and the mean-square voltage is the same as in symmetrical system 1 at the noise intensity 1.6 m/s^2, which suggests a snap-through dominant vibration exists for slight asymmetrical system 2 under the same excitation condition. In experiments, only the intrawell vibrations associated with the deep potential well side are measured. The experimental results show in Fig. 8(b,d) validate the snap-through dominant vibration at high noise intensity because of the high mean-rectified voltage and low mean displacement value. In comparison with the simulation and experiments, the analytical results for system 2 demonstrate the same changing trend as in simulations and experiments and predict a good estimation on the mean-square voltage.

Comparatively, for system 3 with large asymmetry, when under the same excitation condition, the rectified voltage drops substantially in simulations and experiments when the noise intensity is higher than 0.8 m/s^2 as in Fig. 8(c and d), since snap-through vibration amplitudes are not triggered. Here, the mean value of the displacement is large indicating intrawell vibration. This trend is opposite to that of system 1 and 2. The Fourier transforms of the simulated displacement responses for system 3 across the time duration are presented in Fig. 9. The results in Fig. 9(a and b) show the broad range of spectral behaviors as the standard deviation of noise increases from 0 to 2.4 m/s^2. Between 9(a) and (b), the initial conditions are selected to either induce intrawell or snap-through vibration for the simulation start when only harmonic base acceleration occurs. In the time durations near 450–600 s, both simulations show small amplitude vibration that suggests an incapability to sustain snap-through vibration. Yet, still further increase of noise standard deviation such as around 1200 s in Fig. 9 reveals a snap-through-like behavior again. In contrast to the specific phenomena identified for the large asymmetrical system in simulations and experiments, the analysis still indicates a similar snap-through dominant vibration as in systems 1 and 2.

In order to explain the discrepancy between analysis and simulation for greater system asymmetry, three additional cases of asymmetry are considered. System 2 leads to a value for stiffness parameter k_2 of 4 kN/m^2. In the additional asymmetrical systems, the parameter k_2 is changed to 6 kN/m^2, 8 kN/m^2, or 10 kN/m^2. Fig. 7 shows the potential energy shapes for the asymmetrical energy harvesting systems. As shown in Fig. 7, the depth of the potential wells change as a result of the differing asymmetry. With the increase of k_2, the difference between two potential wells depth increases.

For the case that snap-through vibration is frequently induced, the probability distribution function accurately employs the factor of 1/2 for the two distribution functions shown in Eq. (24) so long as the system is symmetric so that the depths of the potential wells are identical. Yet, with the introduction of asymmetry, it is not equally likely that the mean-square displacement will adopt a zero mean value. Consequently, an accommodation is required to characterize amount by which the probability distribution function changes. The Eq. (31) modifies the original distribution in Eq. (24) according to the coefficients p_1 and p_2 which are the potential energies respectively associated with the stable equilibrium position x_1 and x_2. In this way, the cumulative contributions from the two distributions $g(x_{rm}|x_1, \sigma_{xg})$ and $g(x_{rm}|x_2, \sigma_{xg})$, which are Gaussian distributions with mean values x_1 and x_2, account for the asymmetry on an energy basis.

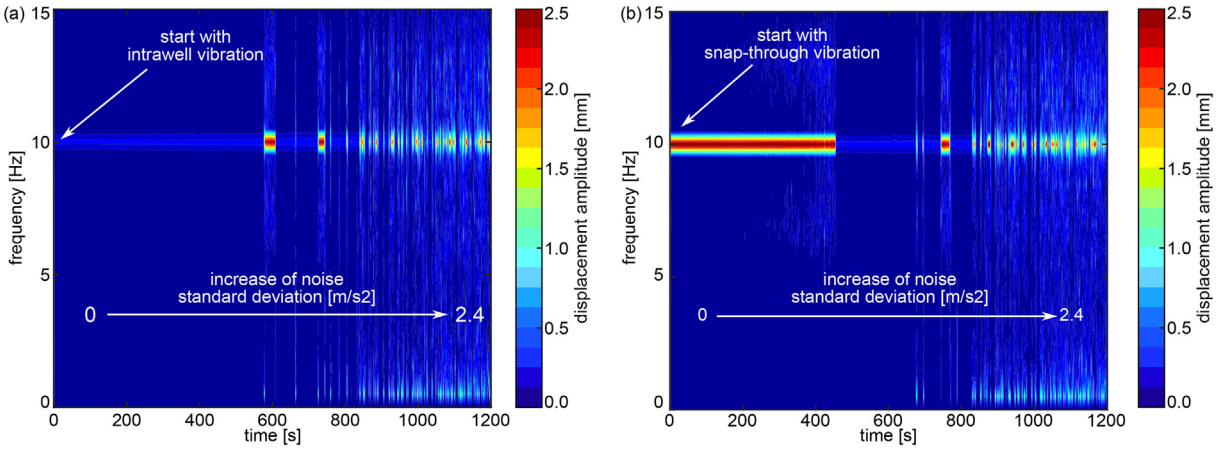

Fig. 9. Short-time Fourier transform of simulated displacement response across the duration with the increase of noise standard deviation for system 3. Response starts with (a) intrawell vibration and (b) snap-through vibration.

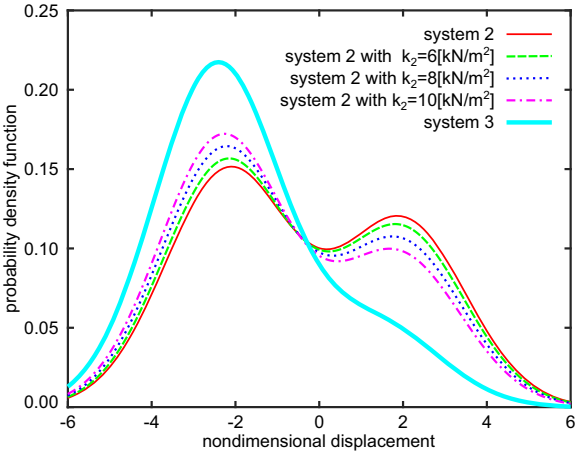

Fig. 10. Probability density functions for the asymmetrical energy harvesting systems.

$$f_3(x_{rm}) = \frac{p_1}{p_1+p_2} g\left(x_{rm}|x_1, \sigma_{xg}\right) + \frac{p_2}{p_1+p_2} g\left(x_{rm}|x_2, \sigma_{xg}\right) \tag{31}$$

Using the expression in Eq. (31) considering that the radicand in Eq. (22b) is a unit valued constant, Fig. 10 presents the probability density functions for the asymmetrical systems when subjected to non-dimensional noise standard deviation $\sigma = 1.5$. The corresponding mean displacement values are numerically integrated through Eq. (31) for the system 2 cases shown in Fig. 10. The mean displacement values are found to be -0.4951 mm for $k_2 = 4$ kN/m^2, -0.7351 mm for $k_2 = 6$ kN/m^2, -0.8852 mm for $k_2 = 8$ kN/m^2, and -1.167 mm for $k_2 = 10$ kN/m^2. The dynamical responses for the systems characterized in Fig. 10 are shown in Fig. 11. At noise standard deviation 2 m/s^2, the mean displacement value from simulations in Fig. 11 are around the mean displacement value calculated from the probability functions and listed above. This validates the energy-weighted coefficients used in the probability density function for asymmetric systems, Eq. (31).

Based on the probability density plots in Fig. 10, for system 3 with large asymmetry there is a much greater possibility to realize intrawell vibration with mean displacements closer to the negative valued equilibrium seen in Fig. 7. Since the increase in asymmetry may increase the contrast between the weighted Gaussian distribution Eq. (23) and the accurate distribution in Eq. (31) as in Figs. 2 and 10, the discrepancies in dynamical responses shown in Figs. 8 and 11 may also increase.

According to these investigations, when under the same excitation condition, vibration energy harvesting systems exploiting nonlinearities yet subjected to ambient vibrations with harmonic and stochastic contributions are susceptible to reduced performance if the nonlinearity is large enough to cause high asymmetry in the potential energy. For robust performance and consistent DC power delivery, it is recommended to reduce asymmetry that may result from nonlinearities in the implementation of energy harvesters in practical vibration environments.

5. Discussion on the dynamic responses

In Section 4, the dynamic responses are investigated using one value for the harmonic base acceleration component. As the potential energy profiles vary with asymmetry such as in Fig. 7, the kinetic energy needed to overcome potential energy barriers and realize snap-through vibration is changed. This indicates that the combination of harmonic and stochastic base accelerations together crucially determine vibration of the energy harvesting system. This section investigates cases in which the distinct dynamic behaviors transition as a result changes in the balance between harmonic and stochastic acceleration components.

Fig. 12 presents the responses for the systems 1, 2, and 3. In Fig. 12, systems 1 and 2 are driven with a harmonic base acceleration of 2.7 m/s^2, while two cases of system 3 are studied using 5 m/s^2 or 8 m/s^2. Comparing the results in Figs. 4(a) and 12(a), with the increase of noise standard deviation σ the mean displacement value for system 1 decreases to be a value around zero, analogous to the unstable equilibrium position around which snap-through occurs. Yet, unlike the trend in Fig. 4(c), for a stochastic base acceleration near 0.7 m/s^2 in Fig. 12(b), the mean square voltage substantially drops. This is similar to the trend shown in Fig. 8(c) for the asymmetric systems and indicates that an intrawell dominant vibration occurs. Such vibration behavior is exemplified in Fig. 13(a) for noise standard deviation 1.6 m/s^2. From Fig. 13(a), although the noise may trigger jumps between the two equilibria, the regularity of generating snap-through vibration is low. A similar trend occurs for system 2 in Fig. 12(a and b) for the smaller value of harmonic base acceleration 2.7 m/s^2.

By contrast, for the harmonic base excitation of 5 m/s^2, the dynamics of system 3 in Fig. 12 suggest a snap-through dominant vibration, based on the larger mean square voltage values for most cases of additive noise base acceleration.

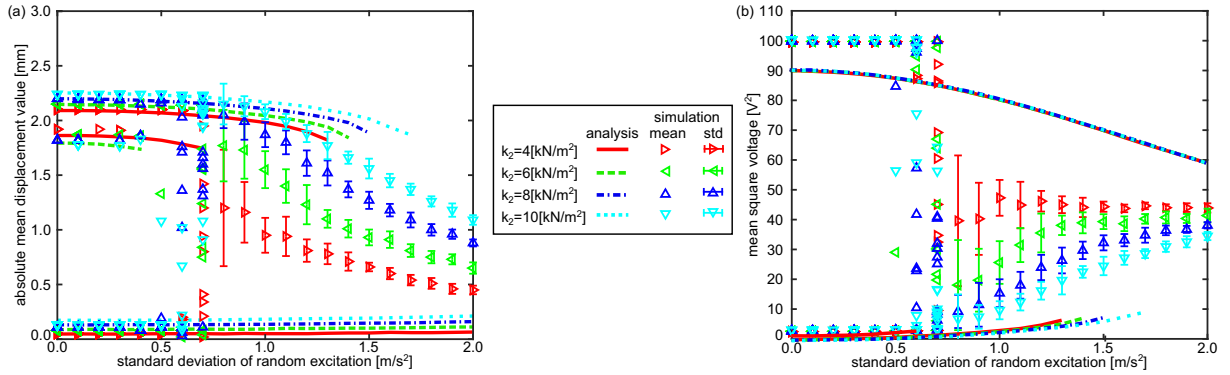

Fig. 11. Analytical and numerical responses for four asymmetrical energy harvesting systems with harmonic amplitude 3.3 m/s^2 and frequency 9 Hz. (a) Absolute mean value of displacement amplitude. (b) Mean square voltage.

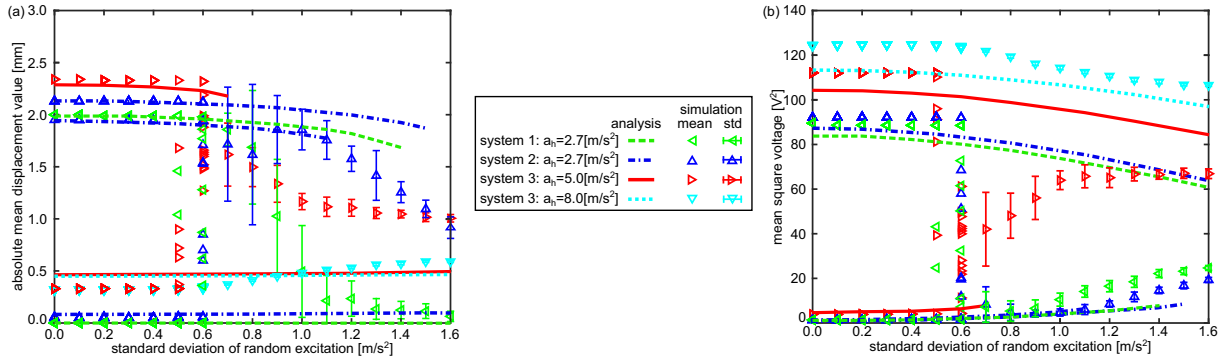

Fig. 12. Analytical and numerical responses for system 1 and 2 at frequency 9 Hz and system 3 at 10 Hz. (a) Absolute mean value of displacement amplitude. (b) Mean square voltage.

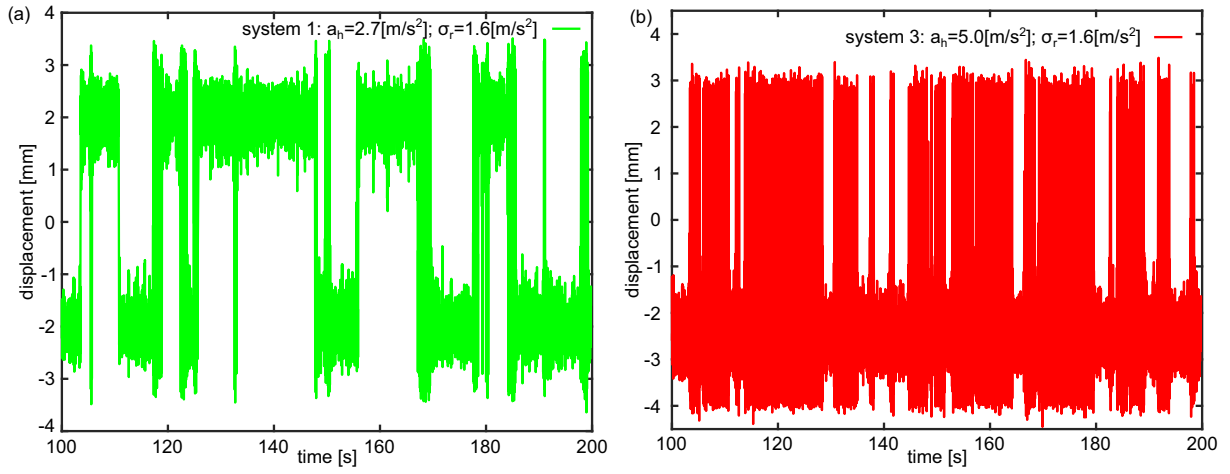

Fig. 13. Transient displacements from simulation considering stochastic base acceleration of 1.6 m/s^2 for (a) system 1 at harmonic excitation 2.7 m/s^2 and (b) system 3 at harmonic excitation 5 m/s^2.

Fig. 13(b) shows a time series of the system 3 when driven by 5.0 m/s^2 harmonic base acceleration and 1.6 m/s^2 standard deviation of stochastic base acceleration. Comparing the analytical and simulation results for the three systems in Figs. 4, 8 and 12, for increase of harmonic base excitation amplitude the discrepancy between simulation and analysis decreases. For instance, for system 3 driven by harmonic base acceleration of 8 m/s^2, the results of Fig. 12 suggest that snap-through

vibration between the stable equilibria is frequently induced. In such case, the discrepancies between the simulation and analysis are lessened.

One explanation for the changes in the discrepancy between analysis and simulation pertains to the influence of the harmonic base acceleration on the effective probability density distribution functions determined by Eq. (24) [31]. With increase in the harmonic excitation component, the possibility of triggering the snap-through vibration is increased. For example, when the harmonic base acceleration for system 3 is 8 m/s^2, snap-through vibration occurs even without presence of stochastic base acceleration. In other words, once stochastic excitation is then introduced, the probability distribution should be similar to that shown in Fig. 2(c) regardless of the standard deviation of the noise. In contrast, when the harmonic base acceleration is too small to generate snap-through vibration, the probability density distribution should intuitively appear like that represented in Fig. 2(a) or Fig. 10. In such latter case, only with increase of stochastic base acceleration should the effective probability distribution function transition to a unimodal distribution. This suggests that for nonlinear energy harvesting systems subjected to combined harmonic and stochastic base excitation, the weighted Gaussian distribution implementation to lead to Eq. (25) results in better estimation of dynamical responses for greater amplitudes of harmonic base acceleration because the response statistics are more comparable to those for a Gaussian distribution [49].

6. Conclusion

This research examines the dynamics of nonlinear energy harvesting systems under combined harmonic and stochastic excitation to demonstrate the influences of asymmetry and relative balance of excitation components on the electrodynamic responses and DC power delivery. An analytical approach based on the equivalent linearization method is established to account for contributions to dynamics from harmonic and stochastic vibration inputs. A weighted Gaussian joint distribution is adopted in the analytical model to improve the accuracy in predicting the statistical responses due to the stochastic excitation. The discrepancies between simulations and analyses are scrutinized thorough study of the probability density distributions. Combined with validation from simulations and experiments, the study reveals that with the increase of noise intensity, the vibration becomes independent on initial conditions, and snap-through or intrawell dominant vibration may occur. Through the investigations, the findings overall suggest that reducing asymmetry or increasing the harmonic excitation component may trigger snap-through dominant vibration for moderate to high standard deviation of stochastic base acceleration. The outcomes help identify robust energy harvesting system design approaches for consistent DC power delivery when the platforms are subjected to realistic vibration environments.

Declaration of competing interest

The authors declare no conflicts of interest in this submission.

Acknowledgments

This research is supported by the National Science Foundation under Award No. 1661572. The authors are grateful to Midé Technology for hardware support.

References

[1] M. Jia, A. Komeily, Y. Wang, R.S. Srinivasan, Adopting Internet of Things for the development of smart buildings: a review of enabling technologies and applications, Autom. ConStruct. 101 (2019) 111–126.
[2] A. Darwish, A.E. Hassanien, M. Elhoseny, A.K. Sangaiah, K. Muhammad, The impact of the hybrid platform of internet of things and cloud computing on healthcare systems: opportunities, challenges, and open problems, Journal of Ambient Intelligence and Humanized Computing (2017) 1–16.
[3] M. Díaz, C. Martín, B. Rubio, State-of-the-art, challenges, and open issues in the integration of Internet of things and cloud computing, J. Netw. Comput. Appl. 67 (2016) 99–117.
[4] L. Reindl, Power Supply for Wireless Sensor Systems, 2018 [Online], http://www.sensornets.org/Documents/Previous_Invited_Speakers/2018/SENSORNETS2018_Reindl.pdf.
[5] A. Hande, R. Bridgelall, B. Zoghi, Vibration energy harvesting for disaster asset monitoring using active RFID tags, Proc. IEEE 98 (9) (2010) 1620–1628.
[6] F. Cottone, H. Vocca, L. Gammaitoni, Nonlinear energy harvesting, Phys. Rev. Lett. 102 (8) (2009), 080601.
[7] A. Erturk, D.J. Inman, Broadband piezoelectric power generation on high-energy orbits of the bistable Duffing oscillator with electromechanical coupling, J. Sound Vib. 330 (10) (2011) 2339–2353.
[8] M. Ferrari, V. Ferrari, M. Guizzetti, B. Andò, S. Baglio, C. Trigona, Improved energy harvesting from wideband vibrations by nonlinear piezoelectric converters, Sensor Actuator Phys. 162 (2) (2010) 425–431.
[9] A. Erturk, J. Hoffmann, D.J. Inman, A piezomagnetoelastic structure for broadband vibration energy harvesting, Appl. Phys. Lett. 94 (25) (2009) 254102.
[10] T. Huguet, M. Lallart, A. Badel, Orbit jump in bistable energy harvesters through buckling level modification, Mech. Syst. Signal Process. 128 (2019) 202–215.
[11] J. Wang, W.H. Liao, Attaining the high-energy orbit of nonlinear energy harvesters by load perturbation, Energy Convers. Manag. 192 (2019) 30–36.
[12] Z. Zhou, W. Qin, W. Du, P. Zhu, Q. Liu, Improving energy harvesting from random excitation by nonlinear flexible bi-stable energy harvester with a variable potential energy function, Mech. Syst. Signal Process. 115 (2019) 162–172.
[13] Q. Wang, N. Wu, Optimal design of a piezoelectric coupled beam for power harvesting, Smart Mater. Struct. 21 (8) (2012), 085013.
[14] R. Hosseini, M. Hamedi, Improvements in energy harvesting capabilities by using different shapes of piezoelectric bimorphs, J. Micromech. Microeng. 25 (12) (2015) 125008.
[15] B. Montazer, U. Sarma, Design and optimization of quadrilateral shaped PVDF cantilever for efficient conversion of energy from ambient vibration, IEEE Sensor. J. 18 (10) (2018) 3977–3988.
[16] J.M. Dietl, E. Garcia, Beam shape optimization for power harvesting, J. Intell. Mater. Syst. Struct. 21 (6) (2010) 633–646.

[17] W. Cai, R.L. Harne, Vibration energy harvesters with optimized geometry, design, and nonlinearity for robust direct current power delivery, Smart Mater. Struct. 28 (7) (2019), 075040.
[18] W. Cai, R.L. Harne, Optimized piezoelectric energy harvesters for performance robust operation in periodic vibration environments, in: Active and Passive Smart Structures and Integrated Systems XII, 2019. Denver,Colorado.
[19] W. Liu, C. Zhao, A. Badel, F. Formosa, Q. Zhu, G. Hu, Compact self-powered synchronous energy extraction circuit design with enhanced performance, Smart Mater. Struct. 27 (4) (2018), 047001.
[20] W. Cai, R.L. Harne, Electrical power management and optimization with nonlinear energy harvesting structures, J. Intell. Mater. Syst. Struct. 30 (2) (2019) 213–227.
[21] E. Lefeuvre, A. Badel, C. Richard, D. Guyomar, Piezoelectric energy harvesting device optimization by synchronous electric charge extraction, J. Intell. Mater. Syst. Struct. 16 (10) (2005) 865–876.
[22] E. Lefeuvre, A. Badel, A. Brenes, S. Seok, C.S. Yoo, Power and frequency bandwidth improvement of piezoelectric energy harvesting devices using phase-shifted synchronous electric charge extraction interface circuit, J. Intell. Mater. Syst. Struct. 28 (20) (2017) 2988–2995.
[23] Q. He, M.F. Daqaq, Influence of potential function asymmetries on the performance of nonlinear energy harvesters under white noise, J. Sound Vib. 333 (2014) 3479–3489.
[24] W. Wang, J. Cao, C.R. Bowen, D.J. Inman, J. Lin, Performance enhancement of nonlinear asymmetric bistable energy harvesting from harmonic, random and human motion excitations, Appl. Phys. Lett. 112 (21) (2018) 213903.
[25] C. Zhang, R.L. Harne, B. Li, K.W. Wang, Statistical quantification of DC power generated by bistable piezoelectric energy harvesters when driven by random excitations, J. Sound Vib. 442 (2019) 770–786.
[26] R.L. Harne, M. Thota, K.W. Wang, Concise and high-fidelity predictive criteria for maximizing performance and robustness of bistable energy harvesters, Appl. Phys. Lett. 102 (5) (2013), 053903.
[27] Y. Chen, M.Q. Feng, C.A. Tan, Modeling of traffic excitation for system identification of bridge structures, Comput. Aided Civ. Infrastruct. Eng. 21 (1) (2006) 57–66.
[28] J.D. Turner, A.J. Pretlove, A study of the spectrum of traffic-induced bridge vibration, J. Sound Vib. 122 (1) (1988) 31–42.
[29] N.D. Anh, N.N. Hieu, The Duffing oscillator under combined periodic and random excitations, Probabilist. Eng. Mech. 30 (2012) 27–36.
[30] R.N. Iyengar, A nonlinear system under combined periodic and random excitation, J. Stat. Phys. 44 (5–6) (1986) 907–920.
[31] Z.L. Huang, W.Q. Zhu, Y. Suzuki, Stochastic averaging of strongly non-linear oscillators under combined harmonic and white-noise excitations, J. Sound Vib. 238 (2) (2000) 233–256.
[32] Y.J. Wu, W.Q. Zhu, Stochastic averaging of strongly nonlinear oscillators under combined harmonic and wide-band noise excitations, J. Vib. Acoust. 130 (5) (2008), 051004.
[33] A.R. Bulsara, K. Lindenberg, K.E. Shuler, Spectral analysis of a nonlinear oscillator driven by random and periodic forces. I. Linearized theory, J. Stat. Phys. 27 (4) (1982) 787–808.
[34] H. Kim, W.C. Tai, J. Parker, L. Zuo, Self-tuning stochastic resonance energy harvesting for rotating systems under modulated noise and its application to smart tires, Mech. Syst. Signal Process. 122 (2019) 769–785.
[35] Q. Dai, R.L. Harne, Investigation of direct current power delivery from nonlinear vibration energy harvesters under combined harmonic and stochastic excitations, J. Intell. Mater. Syst. Struct. 29 (4) (2018) 514–529.
[36] S. Zhou, L. Zuo, Nonlinear dynamic analysis of asymmetric tristable energy harvesters for enhanced energy harvesting, Commun. Nonlinear Sci. Numer. Simulat. 61 (2018) 271–284.
[37] S. Fang, X. Fu, W.H. Liao, Asymmetric plucking bistable energy harvester: modeling and experimental validation, J. Sound Vib. 459 (2019) 114852.
[38] S.F. Ali, S. Adhikari, M.I. Friswell, S. Narayanan, The analysis of piezomagnetoelastic energy harvesters under broadband random excitations, J. Appl. Phys. 109 (7) (2011), 074904.
[39] J. Liang, W.H. Liao, Impedance modeling and analysis for piezoelectric energy harvesting systems, IEEE ASME Trans. Mechatron. 17 (6) (2011) 1145–1157.
[40] Y.C. Shu, I.C. Lien, Analysis of power output for piezoelectric energy harvesting systems, Smart Mater. Struct. 15 (6) (2006) 1499.
[41] W.A. Jiang, L.Q. Chen, Stochastic averaging based on generalized harmonic functions for energy harvesting systems, J. Sound Vib. 377 (2016) 264–283.
[42] Z. Xu, Y.K. Cheung, Averaging method using generalized harmonic functions for strongly non-linear oscillators, J. Sound Vib. 174 (4) (1994) 563–576.
[43] H. Makarem, H.N. Pishkenari, G.R. Vossoughi, A modified Gaussian moment closure method for nonlinear stochastic differential equations, Nonlinear Dynam. 89 (4) (2017) 2609–2620.
[44] H.T. Zhu, S.S. Guo, Periodic response of a Duffing oscillator under combined harmonic and random excitations, J. Vib. Acoust. 137 (4) (2015).
[45] A. Erturk, D.J. Inman, Piezoelectric Energy Harvesting, John Wiley & Sons, Chichester, 2011.
[46] Q. Dai, R.L. Harne, Charging power optimization for nonlinear vibration energy harvesting systems subjected to arbitrary, persistent base excitations, Smart Mater. Struct. 27 (1) (2017), 015011.
[47] J.A. Hansen, C. Penland, Efficient approximate techniques for integrating stochastic differential equations, Mon. Weather Rev. 134 (10) (2006) 3006–3014.
[48] R.L. Harne, K.W. Wang, A review of the recent research on vibration energy harvesting via bistable systems, Smart Mater. Struct. 22 (2) (2013), 023001.
[49] M. Dykman, K. Lindenberg, Fluctuations in nonlinear systems driven by colored noise, in: G.H. Weiss (Ed.), Contemporary Problems in Statistical Physics, SIAM, Philadelphia, 1994 ch. 2.